Acta Cryst. (1983). B39, 210–216

Analysis of the Incommensurate Structure in $Sr_2Nb_2O_7$ by Electron Microscopy and Convergent-Beam Electron Diffraction

BY N. YAMAMOTO†

Department of Physics, Arizona State University, Tempe, Arizona 85287, *USA*

AND K. ISHIZUKA‡

Center for Solid-State Science, Arizona State University, Tempe, Arizona 85287, *USA*

(*Received* 15 *September* 1982; *accepted* 24 *November* 1982)

Abstract

The incommensurate lattice modulation in $Sr_2Nb_2O_7$ has been studied by the high-resolution dark-field technique, which revealed curved lattice fringes showing the irregularity of the modulation wave inside the crystal on a relatively large scale. Convergent-beam electron diffraction patterns were analyzed to derive the symmetry of the incommensurate lattice modulation and that of the fundamental lattice. The results were compared with the previously proposed atom-displacement model.

1. Introduction

Strontium niobate ($Sr_2Nb_2O_7$) is one of the $A_2B_2O_7$-type oxide compounds having a structure composed of slabs of distorted perovskite-type atom blocks (Ishizawa, Marumo, Kawamura & Kimura, 1975). The material undergoes a phase transition at 1615 K from a paraelectric phase with space group *Cmcm* to a ferroelectric phase (normal phase) with the space group $Cmc2_1$ (Nanamatsu, Kimura & Kawamura, 1975). A recent electron-microscope study showed a phase transition to an incommensurate phase at around 493 K (Yamamoto, Yagi, Honjo, Kimura & Kawamura, 1980). In the incommensurate phase a one-dimensional lattice modulation of the displacive type occurs in the [100] direction with a wave vector $\mathbf{q} = (\frac{1}{2} - \delta)\mathbf{a}^*$, where δ is temperature dependent. High-resolution electron microscopy clearly revealed the lattice modulation as reported in a previous paper (Yamamoto, 1982) (hereafter referred to as part I). The atom-displacement model was proposed from an analysis of the systematic extinction of the extra reflections, and the simulated images based on the proposed model were compared to those observed in part I.

Convergent-beam electron diffraction (CBED) is a useful technique to obtain symmetry information from materials from a very small region. General procedures to determine a point group from CBED patterns have been developed by several authors (Goodman, 1975; Buxton, Eades, Steeds & Rackham, 1976). It is sometimes possible to select a space group uniquely by this technique (Tanaka, Saito & Watanabe, 1980; Johnson & Gatehouse, 1980; Bando, Sekikawa, Yamamura & Matsui, 1981). So far the CBED technique has been mainly applied to perfect crystals.

In the present paper the lattice modulation in the incommensurate phase has been studied on a larger scale by means of the high-resolution dark-field technique. The CBED technique is applied to this modulated structure to obtain the symmetry of the incommensurate lattice modulation, the results of which are used to examine an earlier proposed atom-displacement model.

2. Experimental

The specimen preparation was the same as described in part I, except for the [100] specimen plates which were prepared in such a way that the crystals were cut parallel to the (001) plane by a crystal saw, and milled by an Ar-ion beam after mechanical polishing. The specimens were examined with a JEM 200CX electron microscope by the high-resolution dark-field technique. The CBED patterns were taken with a Philips 400T electron microscope at an accelerating voltage of 120 keV. The convergence angles are 3, 7 and 15 mrad for the different condenser aperture sizes, and the probe size is usually about 400 Å in diameter.

† On leave from Physics Department, Tokyo Institute of Technology, Oh-okayama, Meguro-ku, Tokyo 152, Japan.

‡ On leave from Institute for Chemical Research, Kyoto University, Uji, Kyoto-Fu 611, Japan.

0567-7408/83/020210-07$01.50

3. Results

3.1. *Dark-field observation of the lattice modulation*

Fig. 1(*a*) shows the diffraction pattern from a [010] $Sr_2Nb_2O_7$ crystal with the incident beam parallel to the [010] axis. The arrangement of diffraction spots is schematically depicted in Fig. 1(*b*). Fundamental diffraction spots present in the high-temperature normal phase and extra diffraction spots appearing in the incommensurate phase (hereafter called incommensurate diffraction spots) are marked by *F* and *I* in Fig. 1(*b*), respectively. The fundamental reflections have systematic extinctions of *hkl* for $h + k$ odd and *h*0*l* for *l* odd, while the incommensurate reflections have those of $h \pm q,k,l$, $k \neq 0$, for $h + k$ odd and $h \pm q,0,l$ for *h* odd or *l* even. The indices of the reflections are referred to the orthorhombic crystal axes of the normal phase. In addition to the above diffraction spots, very weak spots are seen as indicated by arrows in Fig. 1(*a*). Their intensity changes strongly with varying diffraction conditions. This shows that these diffraction spots appear to be due to multiple scattering. The spots 1 and 4 are kinematically forbidden reflections and are produced by multiple scattering between the fundamental and incommensurate reflections through higher-order Laue-zone reflections. The spots 2 and 5 are mainly produced by scattering among the incommensurate reflections in the zeroth-order Laue zone as indicated by arrows in Fig. 1(*b*). The spot 3 was not observed in the diffraction pattern from the [001] crystal, so the appearance in Fig. 1(*a*) may be due to surface effects, *e.g.* the termination of the crystal with incomplete unit cell as in the case of f.c.c. crystals (Cherns, 1974).

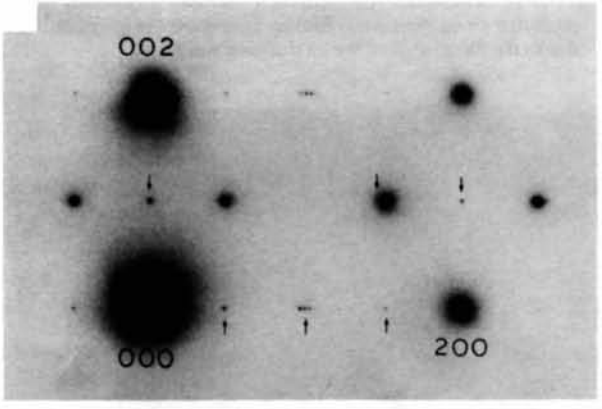

(*a*)

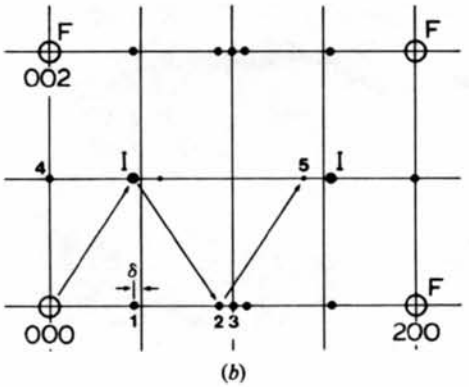

(*b*)

Fig. 1. (*a*) Diffraction pattern of the [010] crystal at room temperature and (*b*) a schematic drawing of (*a*). Arrows in (*a*) indicate weak extra diffraction spots due to the multiple-scattering effect.

Figs. 2(*a*) to (*c*) are dark-field images of the same area of a [010] crystal taken with the objective aperture at 002, $\frac{1}{2}$,0,1 and 100, respectively. No contrast is seen in Fig. 2(*a*) except for a dislocation (*D*) and surface steps (*S*), while bright and dark regions elongated along the *c* axis are seen in Fig. 2(*b*) where fringes nearly perpendicular to the *a* axis appear. The configuration of the bright and dark regions was observed to change with tilting the crystal and also with varying temperature as reported previously (Yamamoto *et al.*, 1980). The fringes have a spacing of about 65 Å, which corresponds to the long period of the modulated lattice (see Fig. 10 in part I), *i.e.* $(4\delta)^{-1}\,\mathbf{a}$, where δ is about 0·015. They are produced by the interference between the incommensurate reflection and the extra reflection of spot 5 (Fig. 1*b*). Fringes with spacing twice that in Fig. 2(*b*) are seen in Fig. 2(*c*). They are produced by the interference between reflections of spots 2 and 3 (Fig. 1*b*). Their spacing and orientation deviate slightly from the average. Some of the fringes terminate and some of them are split into two. The features of these fringes directly reveal the irregularity of the incommensurate lattice modulation in the (010) plane on a relatively large scale. A noticeable fact is that the fringes are not seen in a whole region between some steps as seen in Fig. 2(*c*). This fact suggests that the diffraction spot 3 is produced by the surface effect mentioned before. Fig. 2(*d*) is a high-magnification bright-field image of the area near the position *R*, taken in the [011] orientation (the high-resolution image in this orientation was shown in Fig. 5 of part I). The fringes seen in Fig. 2(*d*) are exactly parallel to the (100) plane with a spacing slightly larger than 2**a**, *i.e.* $(\frac{1}{2} - \delta)^{-1}\,\mathbf{a}$, showing the modulated lattice on a small scale. It should be noted that the fringes in Figs. 2(*b*) and (*c*) are not the images of 'discommensuration arrays' theoretically proposed by McMillan (1976) and recently observed in $TaSe_2$ by electron microscopy (Chen, Gibson & Fleming, 1981; Fung, McKernan, Steeds & Wilson, 1981). If the fringes appearing in Fig. 2(*d*) were these, they should have a spacing of 2**a** in the region between the discommensurations.

Fig. 3(*a*) is a dark-field image of a [001] crystal taken with the objective aperture at the position

indicated by the circle in the diffraction pattern in Fig. 3(*b*). The fringes in two orientations in Fig. 3(*a*) are considered to be produced by interference among the incommensurate reflections inside the objective aperture. Then the angle between the two kinds of fringes can be given as $\alpha = 2\tan^{-1}(2\mathbf{b}/\mathbf{a})\,\delta$. In this case $\alpha = 23{\cdot}0°$ and the corresponding value of δ is 0·015.

The fringes in Fig. 3 are slightly curved and change their contrast from place to place. This indicates the irregularity of the correlation of the modulation wave in successive perovskite-type slabs as schematically depicted in Fig. 4. Solid circles in each perovskite-type slab indicate positions where the phase of the modulation wave at the origin of each unit cell changes by units of π. Oblique lines connecting the solid circles schematically represent the modulated lattice fringes. The irregularity of the fringes may arise in such a way that the phase of the modulation wave in some perovskite-type slabs shifts as indicated by arrows, which causes the curve of the modulated lattice fringes as depicted by broken lines. This irregularity gives rise to the diffuse streaks among the incommensurate diffraction spots aligned along the [010] axis (Fig. 3*b*). The bright and dark contrast seen in Fig. 2(*b*) is considered to be due to this irregularity which acts like a stacking fault to change the intensity of the electron beam.

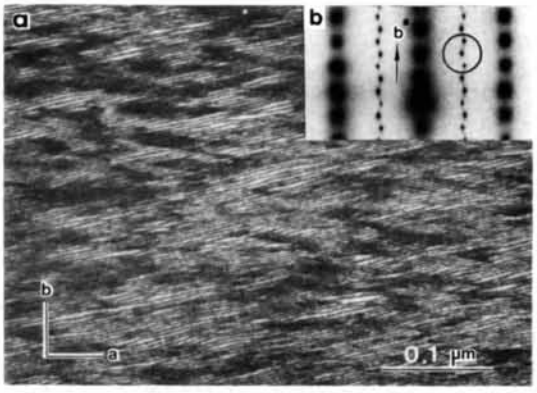

Fig. 3. (*a*) A dark-field image of the [001] crystal and (*b*) the diffraction pattern. The circle in (*b*) indicates the objective aperture used for taking the dark-field image.

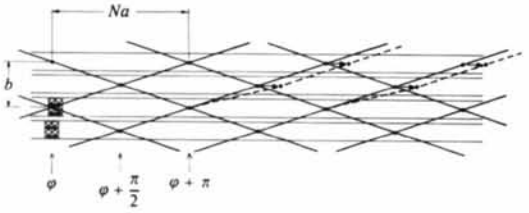

Fig. 4. A schematic representation of the modulated lattice projected along the *c* axis. Broken lines show the irregular lattice due to the phase shift of the modulation wave.

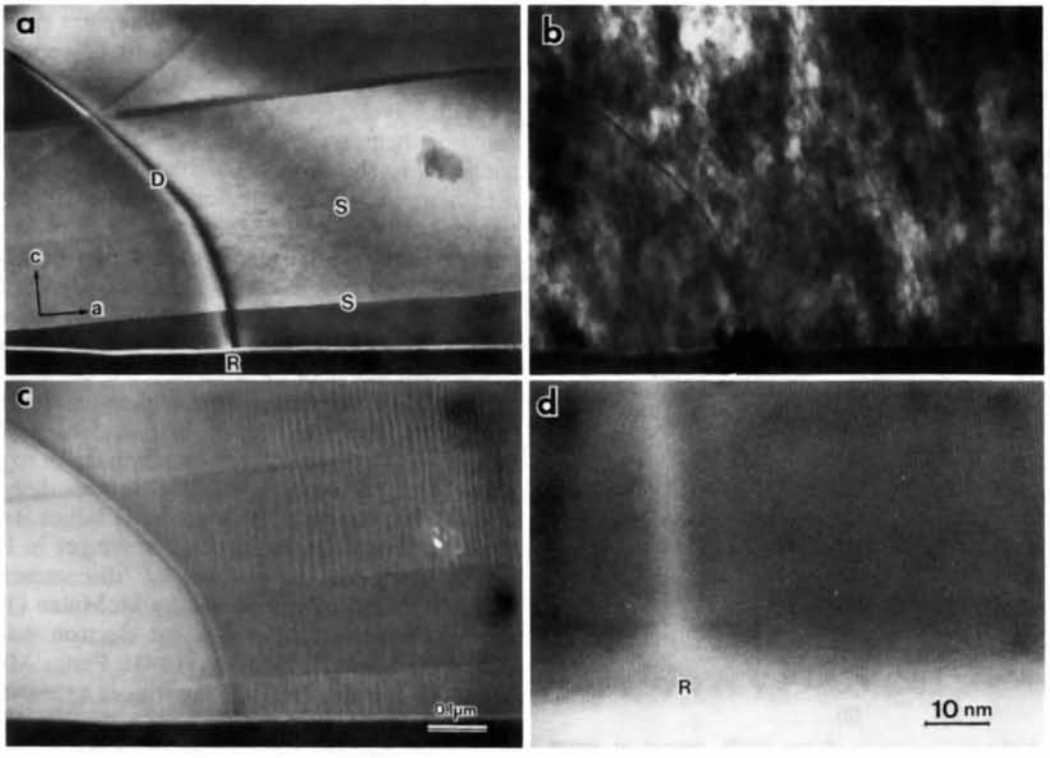

Fig. 2. (*a*) to (*c*) Dark-field images of the [010] crystal taken with the objective aperture positions of 002, $\frac{1}{2}$,0,1 and 100, respectively. (*d*) A high-resolution bright-field image in the [011] orientation. Fringes normal to the *a* axis seen in (*b*) and (*c*) show the incommensurate lattice modulation.

3.2. *CBED patterns*

Figs. 5(*a*) and (*b*) show CBED patterns from a [010] $Sr_2Nb_2O_7$ crystal taken with the incident beam along the [010] direction. The crystal has been cleaved parallel to the (010) plane, so both the entrance and exit surfaces of the crystal are exactly perpendicular to the incident beam, which eliminates the effect of surface inclination on the CBED pattern. The pattern of the incommensurate diffraction disks indicated by arrows change from (*a*) to (*b*) with a small shift of the incident-beam position between the white and dark regions in Fig. 2(*b*), while the patterns of the fundamental diffraction disks remain the same. If only the patterns of the fundamental diffraction disks are considered, there is a mirror plane normal to the a^* axis in the whole pattern. On the other hand, the whole pattern of the incommensurate diffraction disks has a mirror plane normal to the c^* axis. It should be noted that there is an approximate mirror symmetry normal to the c^* axis even for the fundamental diffraction disks.

Fig. 6 shows a [001] zone-axis CBED pattern from the [001] crystal taken with a small convergence angle (3 mrad) in order to avoid the overlap of diffraction disks. The pattern inside each disk has less detail compared to Fig. 5 even from a thick region of the crystal. The whole pattern including fundamental and incommensurate disks is seen to have mirror planes normal to both the a^* and b^* axes, and the total symmetry is *mm*2. CBED patterns with the lower symmetry were sometimes observed both for the fundamental and incommensurate disks, which may be due to the strain field inside the crystal produced during sample preparation.

We treat the patterns of the fundamental and incommensurate diffraction disks separately to examine the symmetry of the CBED pattern. At first we consider the fundamental diffraction disks of the [010] zone axis. The central disk (bright field) shown in Fig. 7(*a*) has symmetry 2*mm*. The disk of the 002 reflection (dark field) (Fig. 7*b*) showed 2*mm* symmetry when it

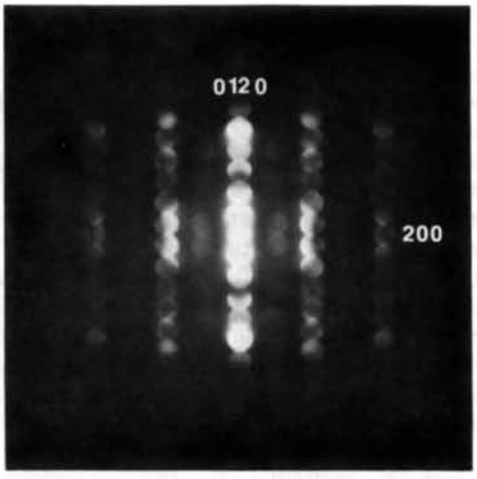

Fig. 6. A CBED pattern taken from the [001] zone axis showing a whole-pattern symmetry of 2*mm*.

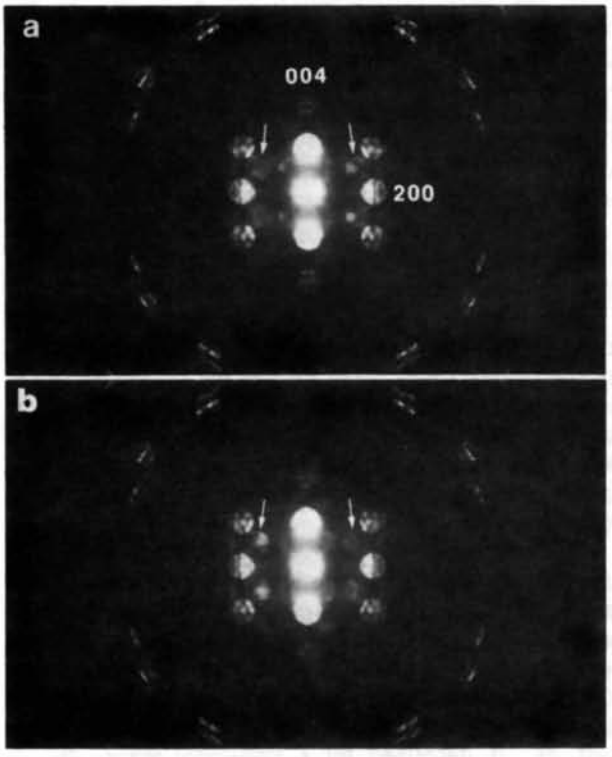

Fig. 5. (*a*) and (*b*) [010] zone-axis CBED patterns taken with different probe positions on a [010] crystal. Patterns of the incommensurate diffraction disks indicated by arrows change from (*a*) to (*b*).

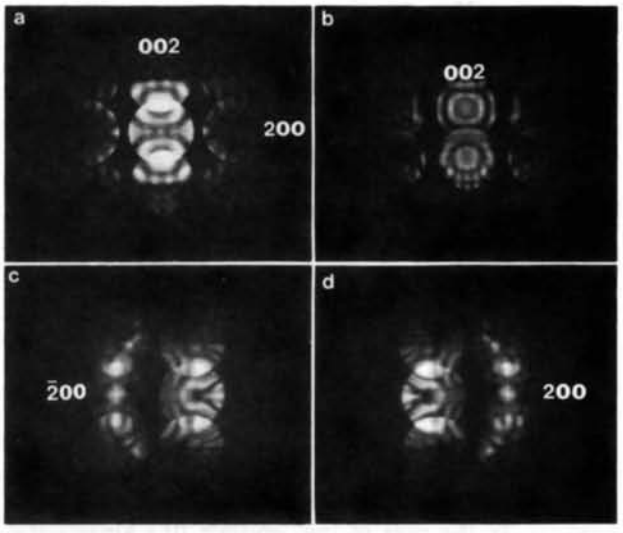

Fig. 7. CBED patterns from a [010] crystal showing symmetries of the fundamental diffraction disks; (*a*) a central disk (bright field), (*b*) a 002 disk (dark field), and (*c*) and (*d*) 200 disks. The reflections concerned are at the Bragg position in each case.

Table 1. *Symmetries of the fundamental and incommensurate diffraction disks in CBED patterns from several zone axes*

$m_{x,y,z}$ are mirrors normal to the a^*, b^* and c^* axes.

Zone axis		*BF*	Whole	*DF*	$\pm G$	Diffraction group
[010]	*F*	2*mm*	m_x	2*mm*	$m1_R$	$m1_R$
	I		m_z	—	—	—
[001]	*F*	2*mm*	2*mm*	—	—	2*mm* or 2*mm*1_R
	I		2*mm*	—	—	
[011]	*F*	m_x	m_x	m_x	*m*	*m*
	I		1	—	—	
[110]	*F*	m_z	1	m_z	m_R	m_R
	I		No reflection			

was at the Bragg position (special case), and the other disks such as the 200 (Fig. 7*d*) and 220 (not shown) reflections showed twofold symmetry at their Bragg positions (general case). The relation between $+G$ and $-G$ disks of the 200 reflections (Figs. 7*c* and *d*) was described by the diffraction group symbol $m1_R$. The same experiments have been done for the other zone axes, and the results are tabulated in Table 1 (only special cases are described for *DF* and $\pm G$ in the table). The point group *mm*2 is derived from the results for the fundamental disks using the table given by Buxton *et al.* (1976). This indicates that the CBED pattern of the fundamental reflections reveals the symmetry of the average structure, which is considered to be the normal phase structure ($Cmc2_1$), without serious effect from the dynamical scattering by the incommensurate reflections.

The intensities of the incommensurate reflections are relatively weak, so it is difficult to examine the symmetry inside the disks at the Bragg position. The whole-pattern symmetries of the incommensurate diffraction disks for several zone axes are also listed in Table 1. As seen in Figs. 5 and 6, there are mirror planes perpendicular to the b^* and c^* axes for the incommensurate diffraction disks. However, it is ambiguous whether a mirror symmetry perpendicular to the a^* axis is present or not since the [001] zone-axis pattern shows it, but the [010] and [011] zone-axis patterns do not. This will be discussed in the next section.

4. Discussion

It is worth considering the possibility of deducing the symmetry of the modulated lattice from the CBED patterns. In the case of thin crystals (the kinematical region), the intensity of the diffraction spots is directly correlated to the structure factor of the crystal, so the fundamental and incommensurate diffraction disks show their own symmetry individually. However, each disk usually has no details inside and the whole pattern shows a center of symmetry due to Friedel's law, even for a noncentrosymmetric crystal. As crystal thickness increases, the multiple scattering effect becomes important. Thus the fundamental and incommensurate reflections interact with each other, and in general there is no assurance that the fundamental and incommensurate diffraction disks indicate the symmetry of each separate lattice correctly.

In the case of $Sr_2Nb_2O_7$, the symmetry of the fundamental diffraction disks is not affected by the presence of the incommensurate reflections as mentioned before. If a pattern of the incommensurate diffraction disks has a different symmetry from the fundamental one, it is safely said that such symmetry comes from the incommensurate lattice alone. For example, no mirror symmetry normal to the a^* axis and a mirror symmetry normal to the c^* axis shown by the incommensurate reflections in the [010] zone-axis pattern are two cases.

The symmetry of the incommensurate diffraction disks in the [001] zone-axis pattern is the same as that of the fundamentals. That reveals the symmetry of the incommensurate lattice itself, since the symmetry of the incommensurate diffraction disks shows the highest symmetry anticipated and cannot become higher as a result of multiple scattering, including the fundamental reflections.

The concept of the ordinary space group cannot be directly applied to the modulated lattice because the atom displacements change from one unit cell to another. In the model proposed in part I, four equivalent atoms at the 4(*a*) sites of the space group $Cmc2_1$ displace with correlation among each other and the displacement vector of the *k*th atom in the *n*th unit cell $\Delta\mathbf{r}_{nk}$ is described by a sinusoidal wave, $\Delta\mathbf{r}_{nk} = \mathbf{A}_k \sin(2\pi n/M + \varphi_k)$. Here M is the period of the modulation wave in units of **a**, and $M = 1/q$. $\mathbf{A}_k$ and φ_k are the amplitude vector and the phase of the *k*th atom.

The values of $\mathbf{A}_k$ and φ_k for all the independent atoms in the unit cell, which were estimated from the previous analysis of the high-resolution images, are tabulated in Table 2.

Here we consider the validity of the atom-displacement model in terms of the CBED-pattern symmetry of the incommensurate diffraction disks. The intensity at each position of a CBED pattern can be given from the following dynamical structure factor $\Psi(\mathbf{h})$, taking account of the multiple scattering processes ($\mathbf{h}_1 \to \mathbf{h}_2 \dashrightarrow \mathbf{h}_n$) (*e.g.* Cowley, 1975):

$$\Psi(hk) = \sum_n \sum_{\mathbf{h}_1} \sum_{\mathbf{h}_2} \cdots \sum_{\mathbf{h}_{n-1}} \sum_{l} F(\mathbf{h}_1) F(\mathbf{h}_2) \cdots F(\mathbf{h}_n) \times Z(\zeta_1, \zeta_2, \ldots, \zeta_n), \quad (1)$$

where $\mathbf{h} = \sum \mathbf{h}_l$, F is a kinematical structure factor of the fundamental or incommensurate reflection and Z is a function of the excitation errors, ζ_1 to ζ_n. Symmetries and dynamical extinction in CBED patterns have been examined theoretically using this equation (Gjønnes & Moodie, 1965; Ishizuka, 1982). We consider scatterings to two positions inside the incommensurate diffraction disks (P and Q in Fig. 8) which are produced by two scattering processes related by mirror symmetry in the zone-axis illumination condition. Here $\mathbf{h}$ is an incommensurate reflection vector. In this case the function Z has the same value for both scattering processes, and the value of Ψ depends only on the kinematical structure factors. The reflections $\{\mathbf{h}_l\}$ involved in the multiple-scattering process must contain an odd number of incommensurate reflections. The multiple-scattering processes mainly contributing to the incommensurate reflection contain only one incommensurate reflection, since the incommensurate reflections are much weaker than the fundamental reflections.

The structure factor of the incommensurate phase can be described as

$$F(\mathbf{s}) = F_f(\mathbf{s}) + F_{\text{inc}}(\mathbf{s}), \quad (2)$$

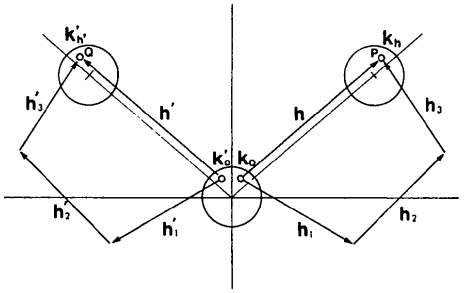

Fig. 8. A schematic diagram of two multiple-scattering processes contributing to intensities at two positions, P and Q, inside the incommensurate diffraction disks in a CBED pattern. The two scattering paths are related by a mirror line normal to the horizontal line. Small circles inside disks indicates directions of the transmitted beams (k_0,k'_0) and reflected beams (k_h,$k'_{h'}$).

where F_f and F_{inc} correspond to the structure factors of the fundamental and incommensurate reflections, respectively, and $\mathbf{s}$ is a scattering vector. The expression for $F_{\text{inc}}(\mathbf{s})$ has been given previously [*e.g.* (5) in part I] and is proportional to the following terms:

$$\begin{aligned} F_{\text{inc}}(\mathbf{s}) &\propto \mp \sum_k^{11} \sum_j^{4} f_k(\mathbf{s}.\mathbf{A}_{kj}) \exp[2\pi i \mathbf{s}.\mathbf{r}_{kj}] \\ &\quad \times \exp[\mp 2\pi i \mathbf{q}.\mathbf{r}_k \mp i\varphi_k] \\ &= \mp \sum_k^{11} f_k(\mathbf{s}.\mathbf{A}_k) \exp[\mp i\varphi_k] \\ &\quad \times \{1 + \exp[\pi i(h+k)]\}(\exp[2\pi i k y_k] \\ &\quad - \exp[-2\pi i k y_k + \pi i l])\exp[2\pi i l z_k] \end{aligned} \quad (3)$$

for $\mathbf{s} = [h \pm q,k,l]$, where f_k is the atom form factor of the kth atom, and the summations with j and k are taken over the four equivalent atoms at the 4(*a*) sites and the eleven independent atoms in the unit cell, respectively. The atom displacement model shown in Table 2 gives the following relations between the structure factors of the incommensurate reflections.

$$h0l;\ F_{\text{inc}}(h \pm q,0,l) = F_{\text{inc}}(\overline{h \pm q},0,l)\exp[\mp i2\varphi_o] \quad (4a)$$

$$hk0;\ F_{\text{inc}}(h \pm q,k,0) = F_{\text{inc}}(\overline{h \pm q},k,0)\exp[\mp i2\varphi_0] \quad (4b)$$

$$= F_{\text{inc}}(h \pm q,\bar{k},0). \quad (4c)$$

The fundamental structure factor F_f is derived from the average structure which has the symmetry of the normal phase as revealed in the fundamental CBED patterns. Then the following relations apply:

$$F_f(hkl) = F_f(\bar{h}kl) = (-1)^l F_f(h\bar{k}l). \quad (5)$$

In the case of [001] zone-axis illumination, the structure factors of the fundamental reflections are symmetrical about the index h, *i.e.* $F_f(hk0) = F_f(\bar{h}k0)$. It is found from this relation and (4*b*), using (1), that the dynamical scattering factor at the position P in Fig.

Table 2. *Amplitude vectors and phases of the modulation waves for the independent atoms in the unit cell, which were derived from the analysis of the high-resolution images in part* I

The atom coordinates are referred to the X-ray data by Ishizawa, Marumo, Kawamura & Kimura (1975).

	x_k	y_k	z_k	A_k	φ_k
Sr(1)	0	0·7059	0·4747	0·03**c**	φ_0
Sr(2)	0	0·4484	0·5377	0·03**c**	φ_0
Nb(1)	0	0·8381	0·5062	0	—
Nb(2)	0	0·0577	0·5348	0	—
O(1)	0	0·007	0·287	0·04**a**	$\varphi_0 + \frac{1}{2}\pi$
O(2)	0	0·113	0·340	0·03**c**	$\varphi_0 + \frac{1}{2}\pi$
O(3)	0	0·650	0·048	0·03**c**	φ_0
O(4)	0	0·213	0·225	0·04**a**	$\varphi_0 + \frac{1}{2}\pi$
O(5)	0	0·799	0·241	0·04**a**	$\varphi_0 + \frac{1}{2}\pi$
O(6)	0	0·908	0·336	0·04**a**	$\varphi_0 + \frac{1}{2}\pi$
O(7)	0	0·450	0·066	0·03**c**	φ_0

8 has the same amplitude as that at Q with a different phase factor $\exp[\mp i2\varphi_0]$, *i.e.*

$$\Psi_P(h \pm q,k,0) = \Psi_Q(\overline{h \pm q},k,0) \exp[\mp i2\varphi_0].$$

Thus the intensities at P and Q are the same, which gives rise to mirror symmetry normal to the a^* axis. The effect of the interaction with the incommensurate reflections in the higher-order Laue zone is neglected, since their contributions are too small. A mirror normal to the b^* axis in the [001] zone-axis pattern or a mirror normal to the a^* axis in the [010] zone-axis pattern can also be derived from (5) and (4*c*) or (4*a*) in the same way. The experimental results show these mirror symmetries except for the last one.

There are some reasons why the expected mirror normal to the a^* axis was not observed in the [010] zone-axis pattern. Dynamical effects may cause the asymmetry, as in the case of a glide plane with a translation parallel to the incident beam, because the cell dimension along the incident beam is relatively large (2·67 nm). However, these effects may not be strong enough to change the disk pattern completely. But the asymmetry in the observed pattern is remarkable. It is plausible to say that the asymmetry is caused by the irregularity of the modulated lattice seen in Figs. 2 and 3. The phase of the modulation wave changes along the thickness direction (the **b** direction) under the [010] zone-axis illumination. This may also explain the dependence of the incommensurate CBED pattern on the probe position as shown in Figs. 5(*a*) and (*b*). The reason why the mirror symmetries hold in the [001] zone-axis pattern is that the modulated lattice is relatively regular along the thickness direction (the **c** direction), as seen in Fig. 2(*b*), and the illuminated area can exclude the irregular region.

The mirror symmetry perpendicular to the c^* axis in the [010] zone-axis pattern is not expected from the above symmetry argument. However, there are mirror planes at $z = 0$ and $\frac{1}{2}$ normal to the c axis in the space group *Cmcm* of the highest-temperature phase above 1615 K, so it is proposed that, although the atoms shift slightly from the mirror planes even in the normal phase, these planes act effectively as glide planes with a translation of **a** in the incommensurate phase if we assume the above atom-displacement model (every atom displaced in the **a** or **c** direction). This is also the reason that the CBED pattern of the fundamental diffraction disks has an approximate mirror symmetry normal to the c^* axis. It is unlikely that the displacements of Sr atoms have an **a** and/or a **b** component, in addition to the **c** component, which would destroy such a pseudo-glide symmetry and also introduce a domain structure because the two different types of displacements become possible. Thus this fact also supports the proposed atom-displacement model.

When we neglect the lattice modulation, *i.e.* $\delta = 0$, space group $Pbn2_1$ is derived from the systematic extinctions of the diffraction spots (both the fundamental and incommensurate spots): $h0l$ for $h + l$ odd; $0kl$ for k odd, assuming the a lattice parameter to be twice that of the fundamental, which agrees with the results of the X-ray analysis by Scheunemann & Müller-Buschbaum (1975). It is noted that when the atoms at the 4(*a*) sites of $Cmc2_1$ change their positions into the 8(*a*) sites of $Pbn2_1$ their displacements must be in the **a** or **c** direction. Our model satisfies this condition.

This work was supported by ARO grant DAAG-29-80-C-0080 and the NSF HREM facility at ASU (grant CHE-7916098).

References

BANDO, Y., SEKIKAWA, Y., YAMAMURA, H. & MATSUI, Y. (1981). *Acta Cryst.* A**37**, 723–728.

BUXTON, B. E., EADES, J. A., STEEDS, J. W., RACKHAM, G. M. (1976). *Philos. Trans. R. Soc. London Ser. A*, **281**, 171–194.

CHEN, C. H., GIBSON, J. M. & FLEMING, R. M. (1981). *Phys. Rev. Lett.* **47**, 723–725.

CHERNS, D. (1974). *Philos. Mag.* **30**, 549–556.

COWLEY, J. M. (1975). *Diffraction Physics*. Amsterdam: North-Holland.

FUNG, K. K., MCKERNAN, S., STEEDS, J. W. & WILSON, J. A. (1981). *J. Phys. C*, **14**, 5417–5432.

GJØNNES, J. & MOODIE, A. F. (1965). *Acta Cryst.* **19**, 65–67.

GOODMAN, P. (1975). *Acta Cryst.* A**31**, 804–810.

ISHIZAWA, N., MARUMO, F., KAWAMURA, T. & KIMURA, M. (1975). *Acta Cryst.* B**31**, 1912–1915.

ISHIZUKA, K. (1982). Proc. 40th Annual EMSA Meeting, Washington, DC, pp. 684–685.

JOHNSON, A. W. S. & GATEHOUSE, B. M. (1980). *Acta Cryst.* B**36**, 523–526.

MCMILLAN, W. L. (1976). *Phys. Rev. B*, **14**, 1496–1502.

NANAMATSU, S., KIMURA, M. & KAWAMURA, T. (1975). *J. Phys. Soc. Jpn*, **38**, 817–824.

SCHEUNEMANN, K. & MÜLLER-BUSCHBAUM, H. (1975). *J. Inorg. Nucl. Chem.* **37**, 1679–1680.

TANAKA, M., SAITO, R. & WATANABE, D. (1980). *Acta Cryst.* A**36**, 350–352.

YAMAMOTO, N. (1982). *Acta Cryst.* A**38**, 780–789.

YAMAMOTO, N., YAGI, K., HONJO, G., KIMURA, M. & KAWAMURA, T. (1980). *J. Phys. Soc. Jpn*, **48**, 185–191.